Efficient control of a switched inertance hydraulic converter with a time-varying load[1]

Chenggang Yuan, Andrew Plummer, Min Pan[2]

Abstract

Digital hydraulics is a novel alternative to proportional or servo-valve-controlled systems in fluid power engineering, providing hydraulic systems with high-energy efficiency, good controllability, and insensitivity to contamination. Switched inertance hydraulic converters (SIHCs) are new digital hydraulic devices that can adjust flow and pressure by digital switching instead of throttling the flow. In this paper, an efficient closed-loop control system is proposed for SIHCs subject to time-varying loading conditions in which the load pressure and/or flow varies with time. The control system is designed to operate SIHCs at optimized switching frequencies and ratios that maximize system efficiency when the load varies. With the proposed controller, the SIHC can effectively adapt to the time-varying load and has achieved up to 10% efficiency improvement and up to 65% pressure ripple reduction without affecting the system's dynamic responses, compared with using a non-optimized controller. The work shows the feasibility and advantages of simultaneously controlling the switching ratio and switching frequency of SIHCs with a time-varying load. As time-varying loading conditions are commonly found in hydraulic applications, the research outcomes constitute an important aspect in the design and development of highly efficient SIHCs and their practical use in hydraulic machinery.

Keywords: Digital hydraulics, Switched inertance hydraulic converters, Hydraulic efficiency, Optimized switching frequency, Time-varying load

---

[1] This article is an extended version of a paper presented at the BATH/ASME 2021 Symposium on Fluid Power and Motion Control [1]

[2] Corresponding author: mp351@bath.ac.uk

1. Introduction

Digital hydraulics is a promising fluid power transmission technology with high energy efficiency, good controllability, and insensitivity to contamination, compared with conventional valve-throttling systems [2-5]. As a branch of digital hydraulics [5, 6], the switched inertance hydraulic converter (SIHC) is mainly comprised of a high-speed switching valve, an inertance tube, and an accumulator, as shown in **Figure 1(a)**, which are analogous to the switch, inductor, and capacitor in the electrical bulk converter as shown in **Figure 1(b)**. The pressure and flow can be converted efficiently with the high-speed switching of the valve, the fluid inertance in the inertance tube, and the capacitance of the accumulator. For example, the delivery flow can be boosted at the expense of lower delivery pressure with the configuration in **Figure 1(a)**, which is named a flow booster. SIHCs are expected to achieve greater than 90% efficiency if friction, valve switching loss, and leakage are small. Programmable control can be realized by using the pulse-width-modulated (PWM) signals to control the high-speed switching valve, as shown in **Figure 1(a)**.

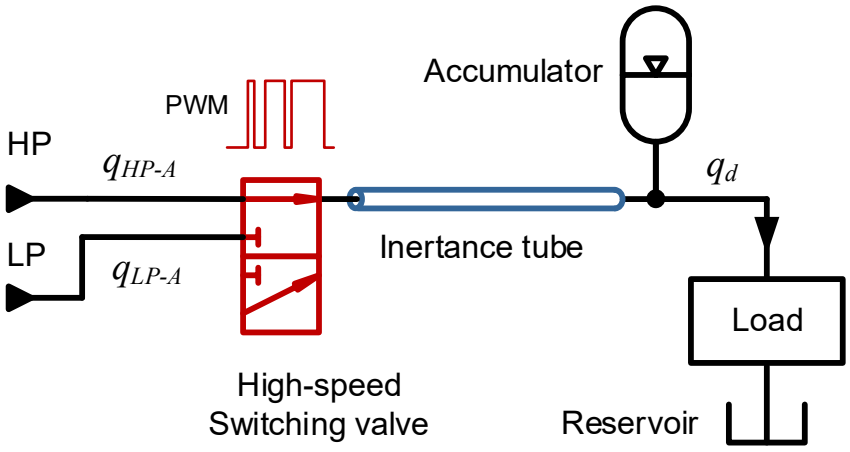

(a) Schematic of a three-port flow booster [7]

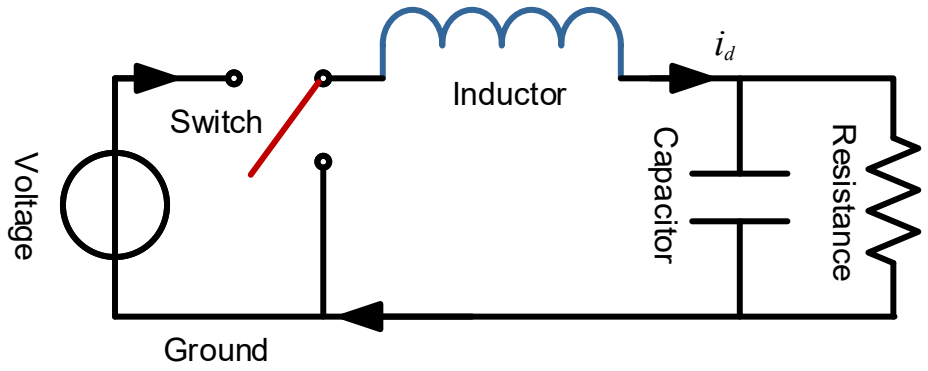

(b) Schematic of an electrical buck converter [8]

Figure 1. Schematic of (a). a three-port flow booster and (b). an electrical buck converter [7, 8]

With the development of digital hydraulics, a series of SIHC configurations including flow booster, pressure booster, switching gyrator, and four-port SIHCs attract significant research interest. It is found that SIHCs have clear potential to improve hydraulic energy efficiency [9-11]. The research group at the Institute of Machine Design and Hydraulic Drives at the Johannes Kepler University Linz, Austria, investigated the characteristics of a hydraulic buck converter (HBC) that uses an on/off valve and a check valve to realize fast switching [12]. For example, the HBC was used to drive a differential cylinder with a mass at a constant switching frequency of 50 Hz. The maximum efficiency improvement was achieved 30% compared with the proportional valve-controlled system [12]. A compact HBC was designed and applied to actuate the robotic leg [13]. The simulated and experimental results showed good angle tracking of the robot leg and 24% lower energy consumption [14-16]. Wang *et al*. at the Centre for Power Transmission and Motion Control at the University of Bath, studied the wave propagation effect in the inertance tube and deduced the optimized switching frequencies of SIHCs [17]. The simulated and experimental results with optimized switching frequencies showed that the wave propagation effect was minimized. To consider the wave propagation effect, Pan *et al*. developed analytical distributed models of a three-port SIHC [8] and enhanced the models with valve switching transition dynamics, nonlinearity, and leakage [18]. The optimized switching frequencies were validated by using the analytical models and experiments, which showed that the system pressure pulsation was reduced and the flow loss was improved by up

to 0.7 l/min at the optimized switching frequencies. The optimized operating conditions were experimentally validated on a flow booster configuration at high switching frequencies with a rotary high-speed switching valve [19]. The results showed that the efficiency was improved by about 5%, compared with using non-optimized switching frequencies. However, current state-of-the-art research on optimizing switching frequencies of SIHCs was conducted at constant load conditions, while the time-varying load is more common in practice and needs to be studied.

This article is an extended version of a paper presented at the BATH/ASME 2021 Symposium on Fluid Power and Motion Control [1], which includes the development of the control system and the experimental validation. In this article, we designed a new control system for SIHCs with a time-varying load to achieve high energy efficiency and investigated system performance in simulation and experiments. Section 2 describes the design of the control system including a Proportional Integral (PI) controller and a switching frequency optimizer, which can vary the switching frequency and switching ratio to minimize the wave propagation effect along the inertance tube. The numerical model of a flow booster with an actuator driving a mass-spring-damper system is developed, and the simulated velocity and force control results are presented in Section 3. The experimental validation of the controller performance was conducted in Section 4, followed by discussions and conclusions.

2. Control system design

To achieve high energy efficiency, a velocity/force control system was designed to operate the flow booster at optimized switching frequencies and switching ratios by integrating a PI controller with a switching frequency optimizer, as shown in **Figure 2**. Based on the demand x_d and feedback x_f (x could be velocity or force), the PI controller outputs the switching ratio α to the switching frequency optimizer, which calculates the optimized switching frequency f_{opt}. The switching ratio output by the PI controller is limited to 10%-90%, which is the effective working range of a flow booster. The anti-windup method of clamping [20] was used to prevent integration wind-up in PID controllers when the switching ratio saturates at 10% and 90%. With the switching ratio α and optimized switching

frequency f_{opt}, the pulse generator generates the PWM signal with varying pulse width and period to control the flow booster with a time-varying load.

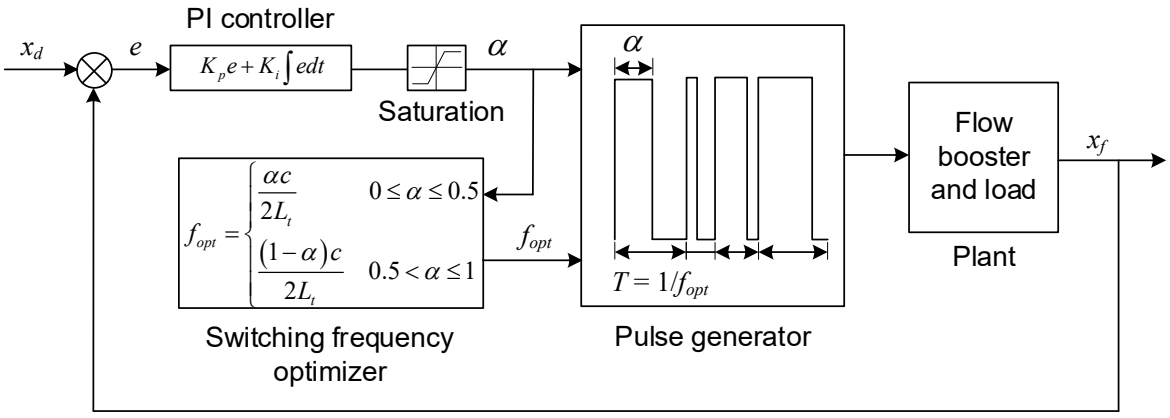

Figure 2. The velocity/force control system consisting of the PI controller and the switching frequency optimizer

The switching frequency optimizer calculates the optimized switching frequencies as [17]:

$$f_{opt} = \begin{cases} \dfrac{\alpha c}{2L_t} & 0 \le \alpha \le 0.5 \\ \dfrac{(1-\alpha)c}{2L_t} & 0.5 < \alpha \le 1 \end{cases} \tag{1}$$

where f_{opt} is the optimized switching frequency, α is the switching ratio, c is the speed of sound, and L_t is the length of the inertance tube. The optimized switching frequency for SIHCs was developed based on minimizing the wave propagation effect along the inertance tube. Ideally, the curve of power loss versus switching ratio is symmetric with respect to α = 0.5 in previous research [8, 17, 18]. For example, the power loss at α = 0.3 equals that at α = 0.7. Therefore, the optimized switching frequency is the same for α and 1 – α, and α = 0.5 is the boundary as in Equation (1).

3. Simulation investigations

3.1 The numerical model of a flow booster

The numerical model of a flow booster is developed, which consists of a 3/2-way high-speed switching valve, an inertance tube, and an accumulator, as shown in **Figure 3**. The valve is modelled as the HP and LP orifices using the standard valve orifice equation, integrated with the valve switching transition characteristics as:

$$q_{HP-A} = C_d A_{HP-A} \sqrt{\frac{2|p_H - p_A|}{\rho}} \operatorname{sgn}(p_H - p_A) \tag{2}$$

$$q_{LP-A} = C_d A_{LP-A} \sqrt{\frac{2|p_L - p_A|}{\rho}} \operatorname{sgn}(p_L - p_A) \tag{3}$$

where $q_{HP\text{-}A}$ and $q_{LP\text{-}A}$ are the flow through the HP and LP orifices, p_H and p_L are the high-supply and low-supply pressures, C_d is the discharge coefficient, $A_{HP\text{-}A}$ and $A_{LP\text{-}A}$ are the HP and LP orifice areas, p_A is the outlet pressure of the switching valve, and ρ is the density of the fluid. A small compressible volume is used between the switching valve and the inertance tube to represent the volume of the valve and a large volume is used to model the downstream accumulator. These volumes are modelled by:

$$p_A = \int \frac{q_{HP-A} + q_{LP-A} - q_A}{V_{up}} B dt \tag{4}$$

$$p_d = \int \frac{q_{end} - q_d}{V_{end}} B dt \tag{5}$$

where p_A and q_A are the outlet pressure and flow of the switching valve, V_{up} and V_{end} are the small and large volumes, p_d and q_d are the delivery pressure and flow, q_{end} is the flow at the outlet of the inertance tube, and B is the bulk modulus of the fluid. The Transmission Line Method (TLM) is used to model the inertance tube. The TLM model was developed by Krus *et al*. [21] and modified by Johnston [22] to include unsteady or frequency-dependent friction, which can accurately and effectively represent wave propagation and laminar friction over a wide frequency range. The details of the model can be found in [22]. The temperature change will affect the bulk modulus and viscosity of the hydraulic oil, which the Transmission Line Method (TLM) relies on to calculate the dissipation number and the speed of sound. The oil temperature has been maintained constant 35 °C in this study to avoid the effect of temperature change.

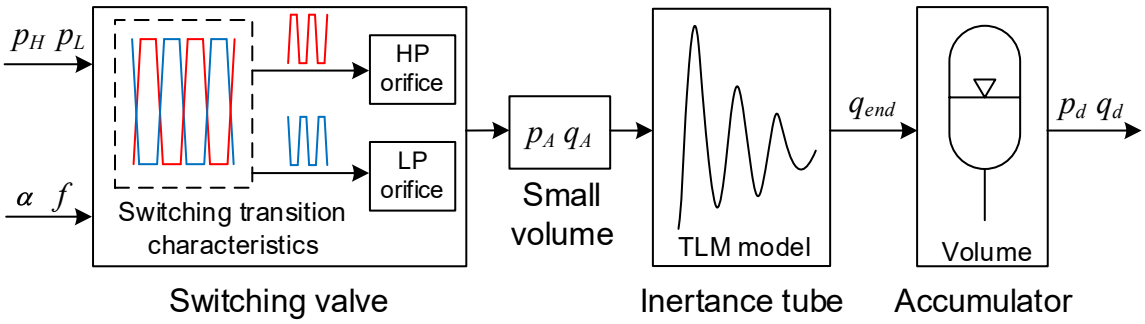

Figure 3. Schematic diagram of the numerical model of a flow booster

3.2 The time-varying load

The flow booster is used to drive a time-varying load that consists of a single-ended cylinder actuating a mass-spring-damper system, as shown in **Figure 4**. The delivery flow of the flow booster q_d is supplied to the piston chamber of the cylinder while the annulus chamber connects to the tank. The mass is attached to the cylinder rod and moves against the spring and the damper. Thus, the required flow, pressure, and actuator force vary with the movement of the mass.

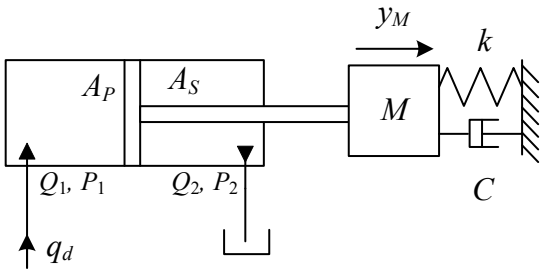

Figure 4. Schematic diagram of the time-varying load

The force balance of the loading system is given by Equation (6):

$$P_1 A_P - P_2 A_S = k y_M + C\dot{y}_M + M\ddot{y}_M \tag{6}$$

where P_1 and P_2 are the pressures of the piston and annulus chambers of the cylinder, A_P and A_S are the piston and annulus areas, M is the load mass, k is the spring constant, C is the viscous friction coefficient, and y_M is the displacement of the actuator.

The piston pressure P_1 and the annulus pressure P_2 are given by Equation (7):

$$P_1 = \int (Q_1 - A_P \dot{y}_M) \frac{B}{V_1} dt$$
$$P_2 = \int -(Q_2 - A_S \dot{y}_M) \frac{B}{V_2} dt \quad (7)$$

where Q_1 and Q_2 are the flow rates into and out of the piston and annulus chambers, respectively of the cylinder, $V_1 = V_P + A_P y_M$ and $V_2 = V_S - A_S y_M$ are the volumes of the piston and annulus chambers considering the chamber volume variations with V_P and V_S being the initial piston and annulus chamber volumes, and B is the bulk modulus of the fluid.

3.3 Results

Velocity and force control of the flow booster with a time-varying loading system were simulated to evaluate the performance of the proposed controller. The parameters listed in **Table 1** were used in simulations. The accuracy of the speed of sound is important to calculate the optimized switching frequency and an accurate method of measuring it in a hydraulic pipeline has been proposed by Johnston and Edge [23]. The method analytically models the pressure ripples using wave equations and experimentally measures the pressure ripples at three locations along the rigid pipeline. The speed of sound is iteratively calculated by minimizing the error between the analytical and experimental results. This method was applied on an SIHC and the undamped speed of sound was estimated to be 1275 m/s, and the damped value was corrected to 1237 m/s with a correction factor of 0.97 considering the viscous effect [19]. The speed of sound of 1237 m/s was used in this work due to the same working conditions, oil properties, and material and diameter of the inertance tube. The load spring stiffness and viscous friction coefficient were identified from experiments, as explained in Section 4.3.

Table 1. Parameters used in numerical simulations

Parameters	Symbol	Value	Unit

Fluid viscosity	υ	30	cSt
Fluid density	ρ	870	kg/m^3
Fluid bulk modulus	B	1.6×10^9	Pa
Speed of sound	c	1237	m/s
High-supply pressure	p_H	60	bar
Low-supply pressure	p_L	20	bar
Inertance tube length including fittings	L	2.06	m
Inertance tube diameter	d	7	mm
Small compressible volume	V_{up}	5	cm^3
Downstream accumulator volume	V_{end}	0.02	m^3
Piston area of the cylinder	A_P	20.25	cm^2
Annulus area of the cylinder	A_S	13.80	cm^2
Load mass	M	890	kg
Load viscous friction coefficient	C	2.365	kN/(m/s)
Load spring stiffness	k	49.14	kN/m

3.3.1 Velocity control

Simulated velocity control results using the optimized controller (a PI controller with the switching frequency optimizer) were presented in **Figure 5** to **Figure 8**. For comparison, the results of using the non-optimized controller (a PI controller with a constant switching frequency of 150 Hz) were also plotted.

Figure 5 shows the velocity response, damping force, and spring force for a step demand of 0.05 m/s. With the optimized controller, the actuation force accelerates the mass to the maximum velocity of 0.22 m/s at 0.2 s as a result of the low spring force and damping force. The mass decelerates with the increasing spring force and reaches at the demand velocity 0.05 m/s after 1.2 s. Small fluctuations occur at the steady state due to the low damping of the loading system. The spring force keeps increasing to 9.5 kN while the damping force is small and constant at a steady state, showing that the

spring effect dominates the time-varying loading system. Compared with the non-optimized controller, the optimized controller achieves a comparable velocity response.

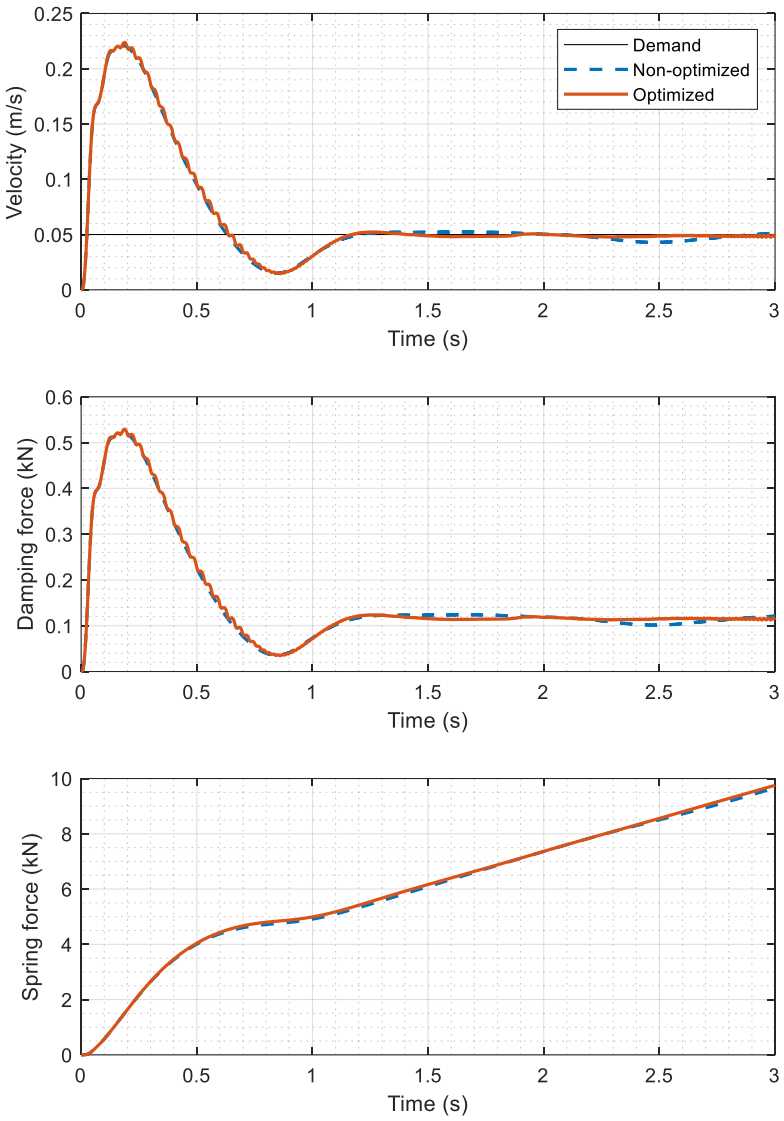

Figure 5. Simulated velocity response, damping force, and the spring force with velocity control

The switching ratio, switching frequency, and efficiency of the flow booster with velocity control are plotted in **Figure 6**. The switching ratio with the optimized controller is constant at the lower limit of 10% for about 0.6 s to decelerate the mass and increases to 85% to deliver high pressure to overcome the increasing spring force at 3 s. Accordingly, the optimized switching frequency keeps constant at 30 Hz before increasing to 150 Hz and decreasing to 50 Hz. The system efficiency η is calculated as:

$$\eta = \frac{p_d q_d}{p_H q_H + p_L q_L} \times 100\% \tag{8}$$

where p_d, p_H, and p_L are the delivery pressure, high-supply pressure, and low-supply pressure, and q_d, q_H, and q_L are the delivery flow rate, high-supply flow rate, and low-supply flow rate. The non-optimized efficiency varies from 20% to 80%, while the optimized efficiency is maintained above 50% and significantly improved by up to 28% (from 22% to 50% at 0.85 s), showing the advantage of using the optimized controller.

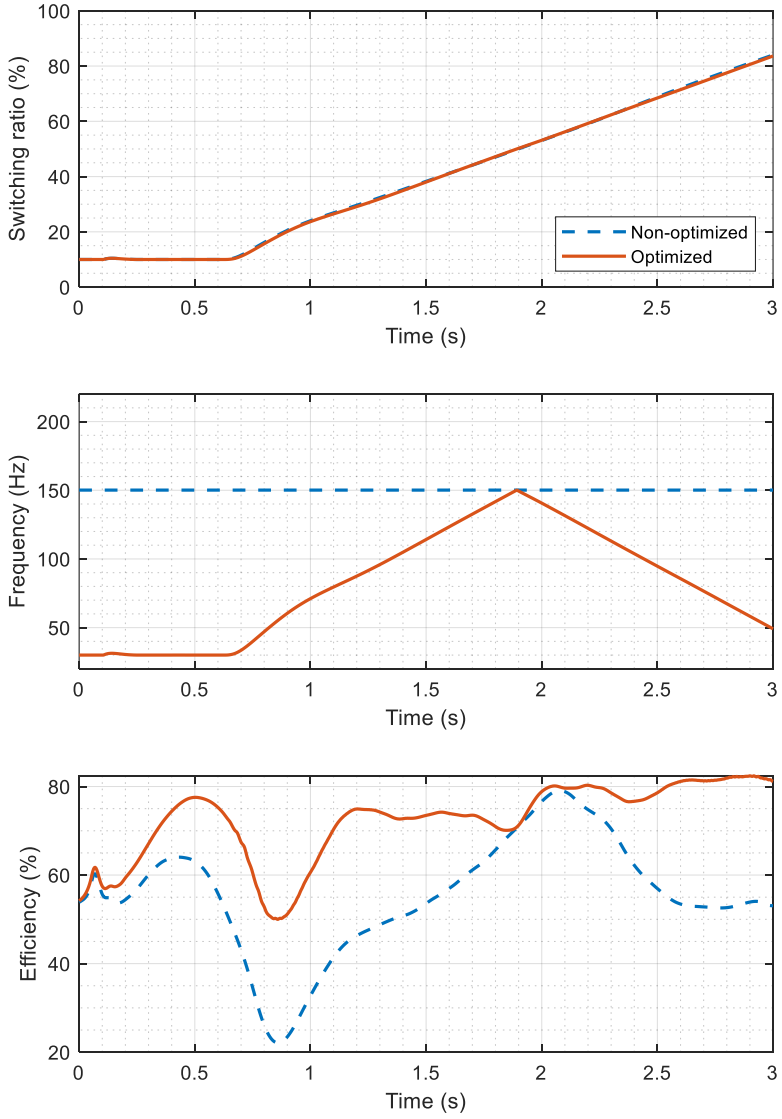

Figure 6. Simulated switching ratio, switching frequency, and efficiency of the flow booster with velocity control

The delivery pressure and flow rate with velocity control are shown in **Figure 7**. The delivery pressure of the non-optimized result keeps increasing to 50 bar to drive the mass against the spring. The zoom-in plot shows a significant reduction of pressure ripple (up to 55% of peak-to-peak value) with the optimized controller. However, the pressure ripples are not reduced for 0.1-0.8 s because of the low switching frequency of 30 Hz. The delivery flow rate of the non-optimized result reaches a steady state with flow ripples up to 20 l/min (peak-to-peak value), after a large transition overshoot of 30 l/min. The flow ripples with the optimized controller are significantly reduced by up to 62% (peak-to-peak value), as shown in the zoom-in plot. The results validate that the optimized controller can effectively reduce flow and pressure ripple with the minimization of the wave propagation effect, which leads to higher efficiency compared with the non-optimized controller.

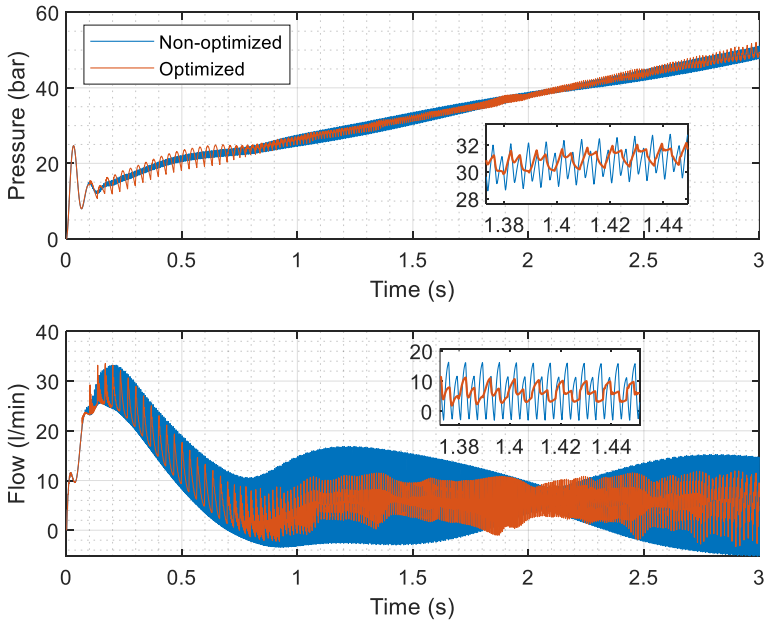

Figure 7. Simulated delivery pressure and flow rate of the flow booster with velocity control

The piston and annulus pressures and actuator position are shown in **Figure 8**. For the optimized result, the piston pressure increases to 48.5 bar at 3 s with the movement of the mass while the annulus pressure increases to 2 bar before decreasing to a small value (< 0.5 bar) in the steady state.

It is noticed that the actuator position at 3 s is 0.002 m further in the optimized result. This is because more work has been done in 3 s due to the improved efficiency of using the optimized controller.

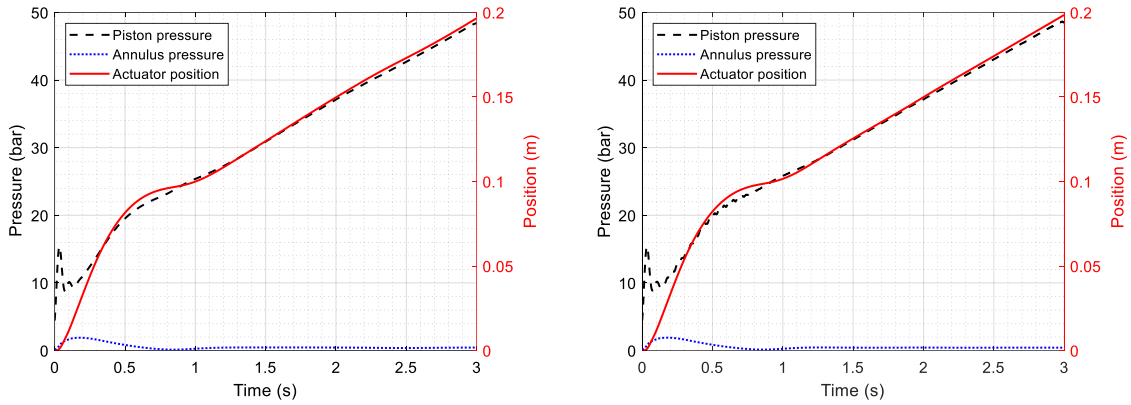

(a) Non-optimized (b) Optimized

Figure 8. Simulated piston and annulus pressures and actuator position with velocity control

3.3.2 Force control

Force control was simulated using the proposed controller (optimized) and the PI controller with a constant switching frequency of 150Hz (non-optimized). The results were presented and compared in **Figure 9** to **Figure 12**.

Figure 9 shows the force response, damping force, and spring force with force control. A settling time (2%) of 0.9 s and an overshoot of 3% have been achieved by using the optimized controller. The damping force increases to 0.7 kN at 0.3 s and gradually decreases to zero after 2 s while the spring force overshoots to 9.5 kN at 1.1 s before achieving the demand force of 9 kN at the steady state. At the beginning, the mass accelerates due to the low damping and spring force and decelerates with the increase of the spring force. Eventually, the mass stops when the spring force is balanced with the demand actuator force and the damping force becomes zero. There is no significant difference between the optimized and non-optimized results, which means the optimized controller can achieve a comparable force dynamic response.

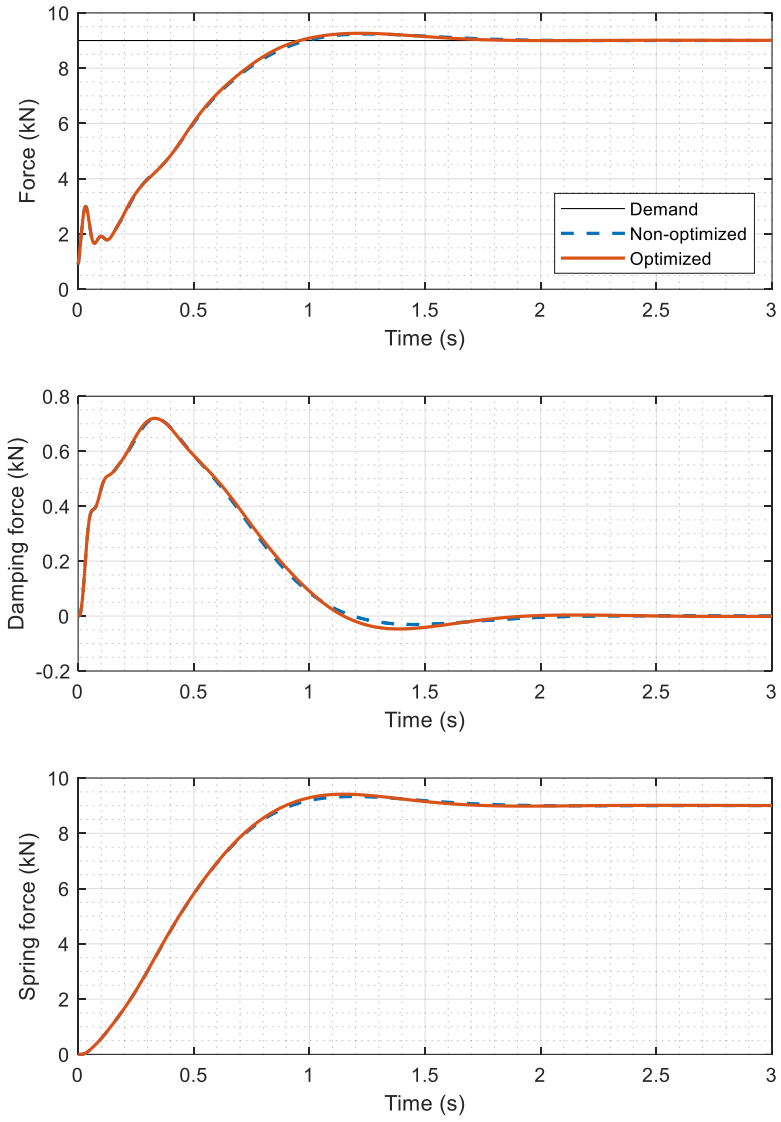

Figure 9. Simulated force response, damping force, and spring force with force control

The switching ratio, switching frequency, and efficiency of the flow booster with force control are shown in **Figure 10**. The switching ratio with the optimized controller increases to 70% at 0.5 s and decrease to about 62% after 1 s to maintain the demand force. As a result, the optimized switching frequency increases to 150 Hz within 0.15 s before decreasing to 110 Hz at 1.5 s. With the optimized switching frequency, the efficiency has been improved by up to 30% at 0.5-1.2 s before the mass stops and the efficiency becomes zero, compared with the result with the non-optimized controller.

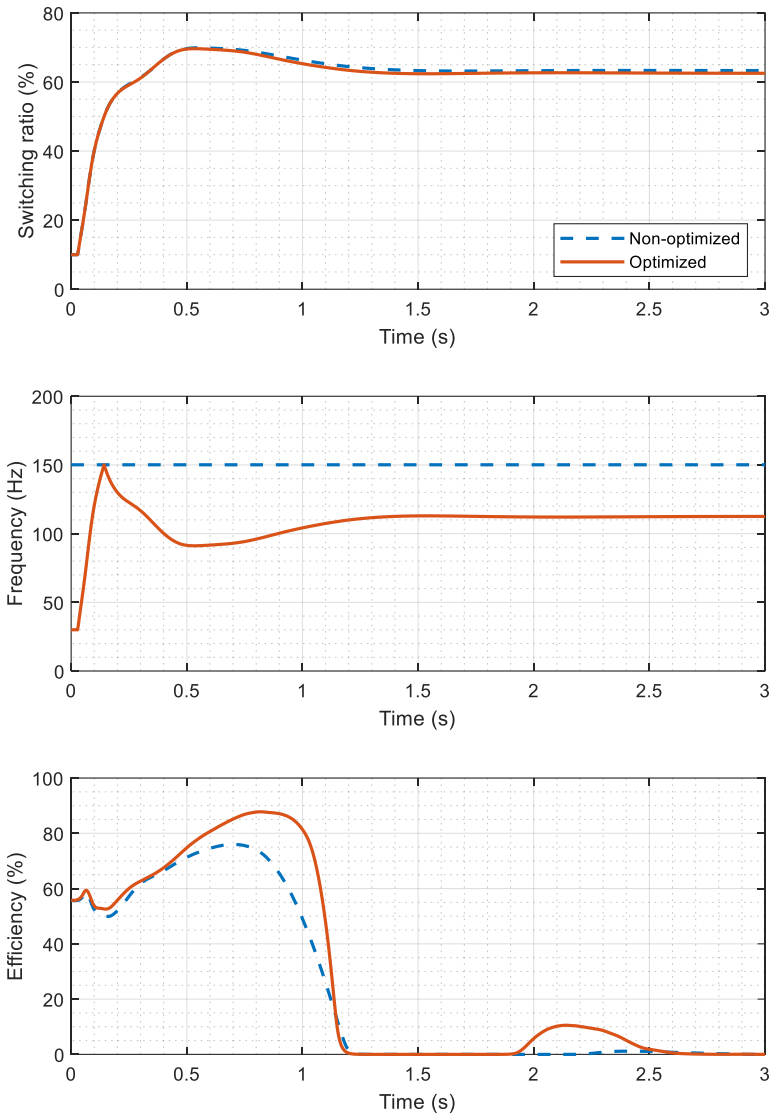

Figure 10. Simulated switching ratio, switching frequency, and efficiency of the flow booster with force control

Figure 11 shows the delivery pressure and flow rate of the flow booster with force control. For the optimized results, the mean delivery pressure increases to 46 bar at 1 s before achieving the steady-state pressure of 44 bar to maintain the demand force, and the mean delivery flow rate increases to the maximum value of 38 l/min at 0.35 s before decreasing to 0 l/min. The optimized controller achieves up to 48% and 66% reduction in pressure ripple and flow ripple, respectively, compared with the non-optimized controller as shown in the zoom-in plots.

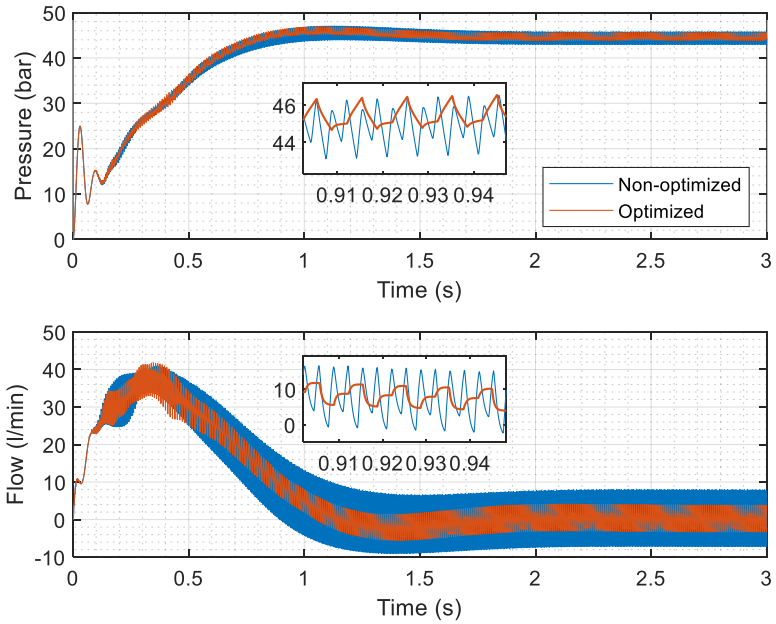

Figure 11. Simulated delivery pressure and flow rate of the flow booster with force control

The piston and annulus pressures and actuator position with the non-optimized and optimized controllers are shown in **Figure 12**. The use of the optimized controller does not cause significant change to the actuator pressures and position compared with the non-optimized controller. The only noticeable difference is that the piston pressure and the actuator position of the optimized result reach the steady state 0.2 s quicker than that of the non-optimized result. This is because for the same amount of work of moving the mass to the balanced position (system steady state), the system with the optimized controller moves the mass more quickly due to higher efficiency.

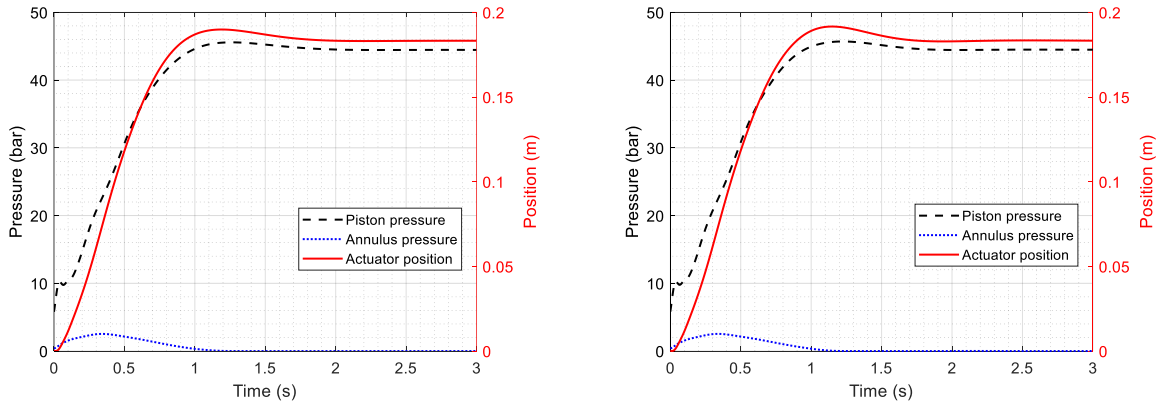

(a) Non-optimized (b) Optimized

Figure 12. Simulated piston and annulus pressures and actuator position with force control

4. Experimental study

4.1 Experimental testing rig

Figure 13(a) shows the schematic of the experimental test rig, in which a flow booster is connected to a time-varying loading system and a controller. A hydraulic power pack including two gear pumps with a maximum supply pressure of 100 bar and 50 bar are used as HP and LP supplies. Three accumulators and three shock suppressors (Inline Pulse-Tone™ Shock Suppressors, Parker Hannifin) are used to eliminate the pressure pulsations. The charging pressures of the HP, LP, and downstream accumulators are 45 bar, 15 bar, and 30 bar. The charging pressures of the shock suppressors are 22.5 bar, 7.5 bar, and 15 bar, respectively. A high-speed rotary valve developed at the University of Bath [19, 24] is used as the switching valve to vary the switching frequency and switching ratio simultaneously. The switching frequency is controlled by a brushless servomotor (Baldor BSM50N-375AF) with a maximum speed of 5100 rpm and the switching ratio is controlled by a stepper motor (stepIM NEMA34). Three miniature piezoresistive dynamic pressure transducers (Measurement Specialties XP5 series) are used to measure the pressures of the HP and LP port of the valve, and the delivery pressure at the outlet of the inertance tube (The transducers ranges from 0-350 bar, 0-70 bar, and 0-200 bar, respectively). A gear flow meter (0.5-70 l/min, ZHM series from KEM) is used to measure the dynamic high-supply flow rates. A turbine flow meter (HYDAC, 6-60 l/min) is used to measure the delivery flow rate at the outlet of the inertance tube.

The time-varying loading system is a mass-spring-damper system including a single-ended cylinder, a trolley (mass), and a spring. The delivery flow of the flow booster is supplied to the piston chamber of the single-ended cylinder while the annulus chamber is connected to the reservoir. Two pressure transducers (DRUCK PDCR 610) with a range of 0-200 bar are used to measure the piston and annulus pressures. The mass of the trolley is 890 kg and the stroke of the cylinder is 0.61 m. The trolley moves against the spring at the end of the stroke between 0.42 m and 0.61 m. A wirewound

potentiometer (RAYELCO PT420) is used to measure the actuator position. The spring stiffness and viscous friction coefficient of the system are experimentally identified as 49.14 kN/m and 2.365 kN/(m/s) as explained in Section 4.3. The damping approximates the effect of flow restriction in cylinder connections and the dynamic friction between the piston and the cylinder wall.

The designed controller was implemented on a Simulink Real-Time target PC with a NI-6251 card for A/D and D/A conversion. The delivery pressure and flow, the actuator position, and the piston and annulus pressures are input to the controller. The controller outputs the optimized switching ratio and switching frequency to control the position and speed (respectively) of the two motors, which form part of the high-speed switching valve. **Figure 13(b)** and **(c)** show photographs of the flow booster and the time-varying loading system. The parameters listed in **Table 1** for simulation are also applicable to the experiments.

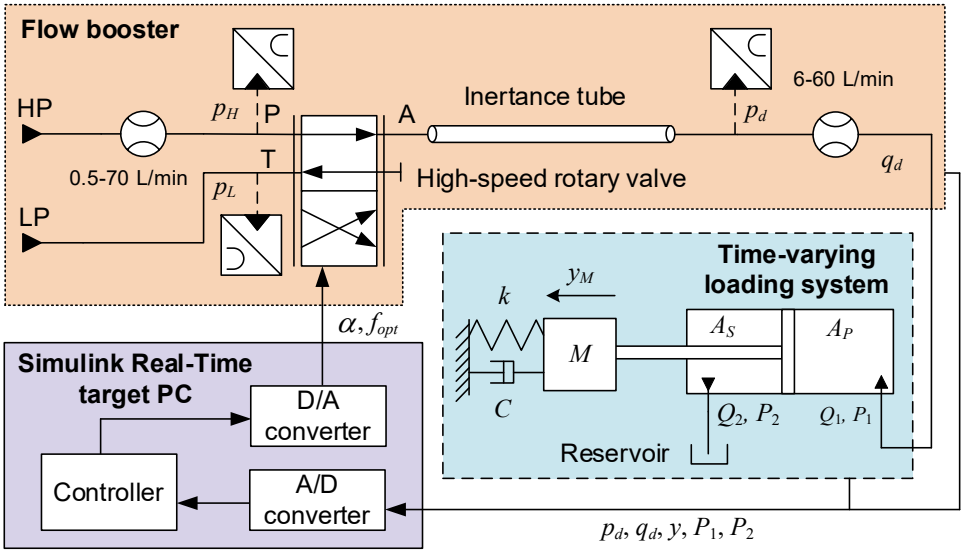

(a) Schematic of the test rig

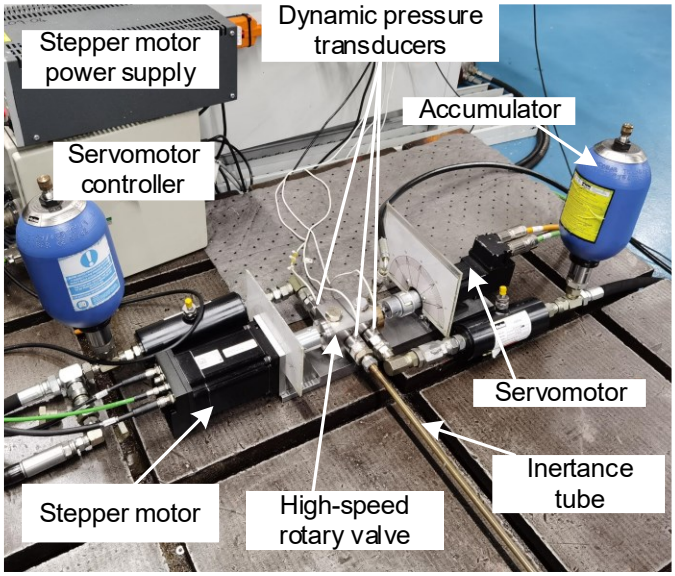

(b) Photograph of the flow booster

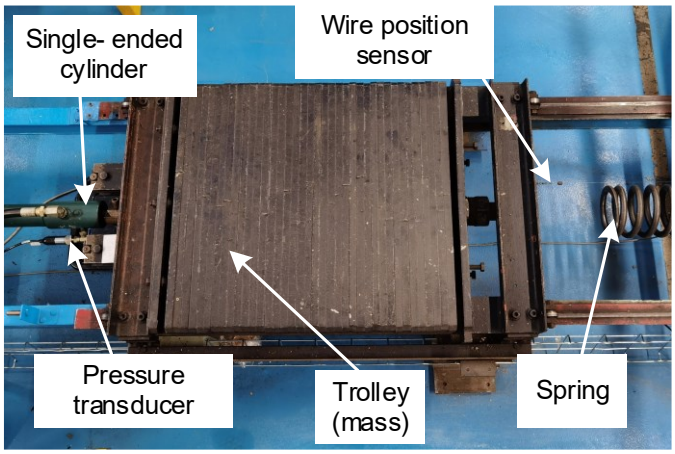

(c) Photograph of the time-varying loading system

Figure 13. Experimental rig of a flow booster driving a time-varying loading system

4.2 Optimized switching frequency validation with a constant load

The flow booster was operated at 150 Hz and optimized switching frequencies for switching ratios of 0-100% at a constant delivery flow rate of 14 l/min. The optimized switching frequencies were calculated using Equation (1), and the lower limit of 30 Hz was used for 0% and 100%. The flow losses and efficiencies are presented in **Figure 14**. The flow loss is defined as the difference between the average high-pressure supply flow rate and the ideal high-pressure supply flow rate: $q_{loss} = \bar{q}_H - q_d \alpha$ as in [8]. Compared with the results of 150 Hz, the flow losses of the optimized

results are significantly improved, by about 1.2 l/min and 3.6 l/min at the low and high switching ratio ranges of 10%-40% and 70%-90%, respectively, as shown in **Figure 14(a)**. **Figure 14(b)** shows that the efficiency is significantly improved by up to 12% and 10% at switching ratios of 15% and 75% with optimized switching frequencies. The improved flow losses and efficiencies validate the advantage of using the optimized switching frequency for the flow booster with a constant load.

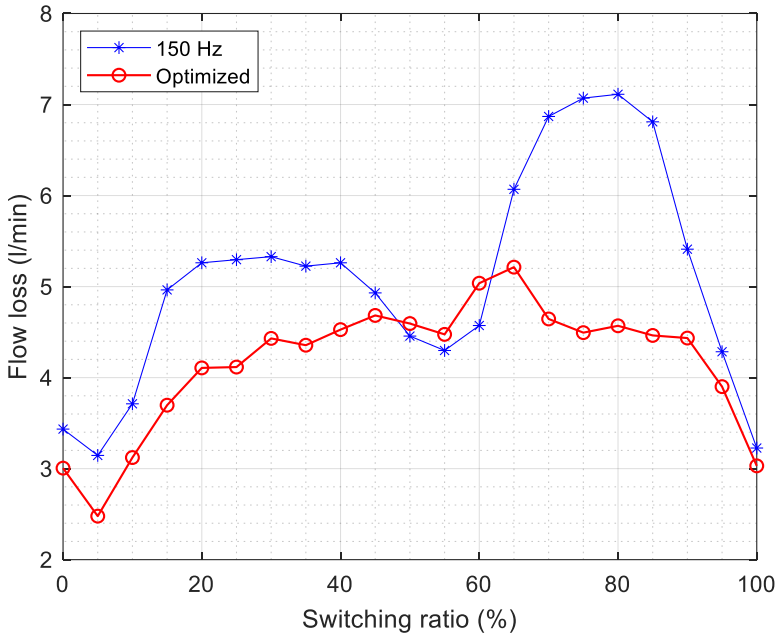

(a) Flow losses

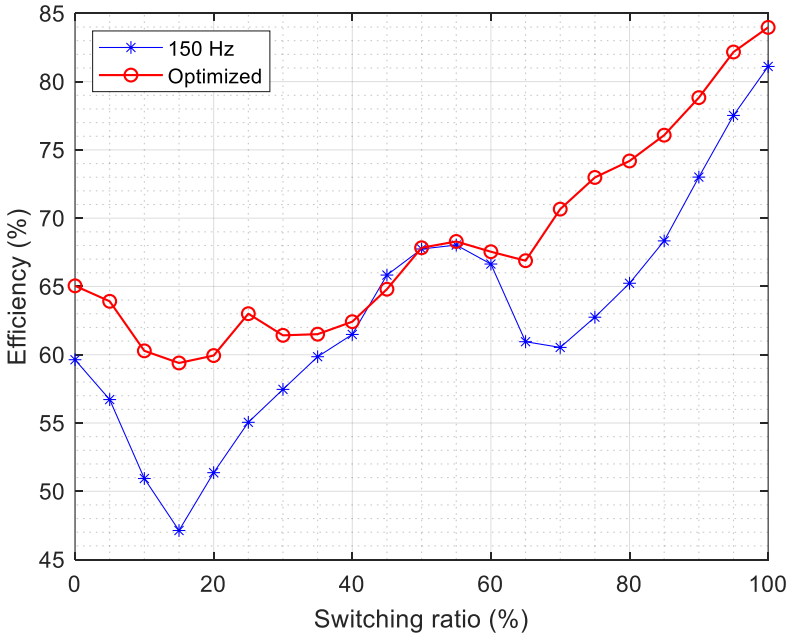

(b) Efficiencies

Figure 14. (a). Flow losses and (b). efficiencies of the flow booster at a constant delivery flow rate of 14 l/min

4.3 Viscous friction coefficient and spring stiffness identification

Figure 15 shows the piston and annulus pressures and the actuator position of the time-varying loading system operated at a velocity of 0.03 m/s. Initially, the mass is not in contact with the spring and the actuation force is balanced with the damping force before the actuator starts to compress the spring at 24 s as given by:

$$P_1 A_P - P_2 A_S = F_{damp} \tag{9}$$

where F_{damp} is the damping force. The viscous friction coefficient can be estimated from:

$$C = \frac{F_{damp}}{\dot{y}_M} \tag{10}$$

where $\dot{y}_M$ is the velocity of the actuator. After 24 s, the actuator force is balanced with the damping force and the spring force when the trolley compresses the spring, as given by:

$$P_1 A_P - P_2 A_S = F_{damp} + F_{spring} \tag{11}$$

where $F_{spring} = k(y_M - y_{M0})$ is the spring force, and y_{M0} = 0.42 m is the position where the trolley starts to compress the spring. Taking the two points at 24 s and 27 s as shown in **Figure 15**, the spring stiffness can be estimated from:

$$k = \frac{\Delta P_1 A_P - \Delta P_2 A_S}{\Delta y_M} \tag{12}$$

where ΔP_1 is the piston pressure difference between the two points, $\Delta P_2 = 0$ because the annulus pressure is constant, and Δy_M is the position difference between the two points.

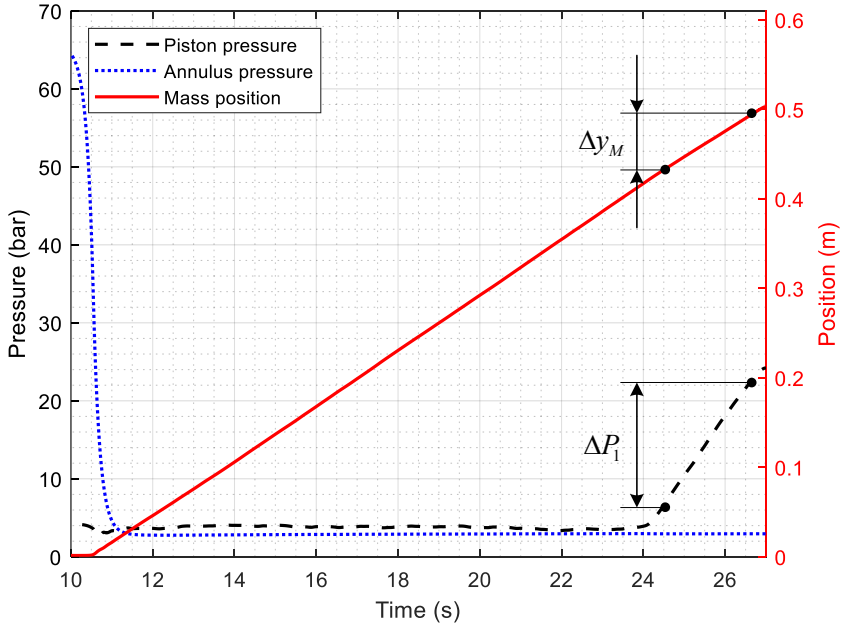

Figure 15. Piston and annulus pressures and the actuator position at a velocity of 0.03 m/s

The time-varying loading system was tested at velocities between 0.03 m/s and 0.3 m/s to identify the system viscous friction coefficient and the spring stiffness. The damping force is small compared with the spring force; hence the viscous friction coefficient is assumed to be constant at the mean value of the tests for simplification. The mean values of the viscous friction coefficients and spring stiffnesses are 0.236 kN/(m/s) and 49.14 kN/m using Equation (9)-(12) from the tests.

4.4 Control of the time-varying loading system

The proposed controller was validated experimentally. The flow booster is connected to the time-varying loading system by a tandem center directional control valve (TDCV) to extend and retract the trolley during experimental work. The trolley is driven by the flow booster from the initial position of 0.42 m where it starts to compress the spring. The results of velocity control and force control with the proposed controller are presented (optimized) and compared with results from a PI controller with a constant switching frequency of 150 Hz (non-optimized).

4.4.1 Velocity control

Figure 16 shows the experimental velocity response, damping force, and spring force with velocity control. The derivative of the actuator position was used as the velocity signal for the controller and filtered by a Butterworth filter with a cut-off frequency of 15 Hz to reduce the noise. The velocity control experiments were conducted at a demand value of 0.05 m/s. The controller was turned on at 0 s and the TDCV was opened at 0.3 s. The trolley accelerates with a large overshoot to 0.24 m/s at 0.4 s due to the small spring force and damping force, before achieving the demand velocity of 0.05 m/s after 0.9 s. Oscillations occur at the steady state for 1-3 s due to the low damping of the loading system. The optimized controller achieves a velocity response comparable to the non-optimized controller without significant effects on the damping force and spring force of the mass-spring-damper system.

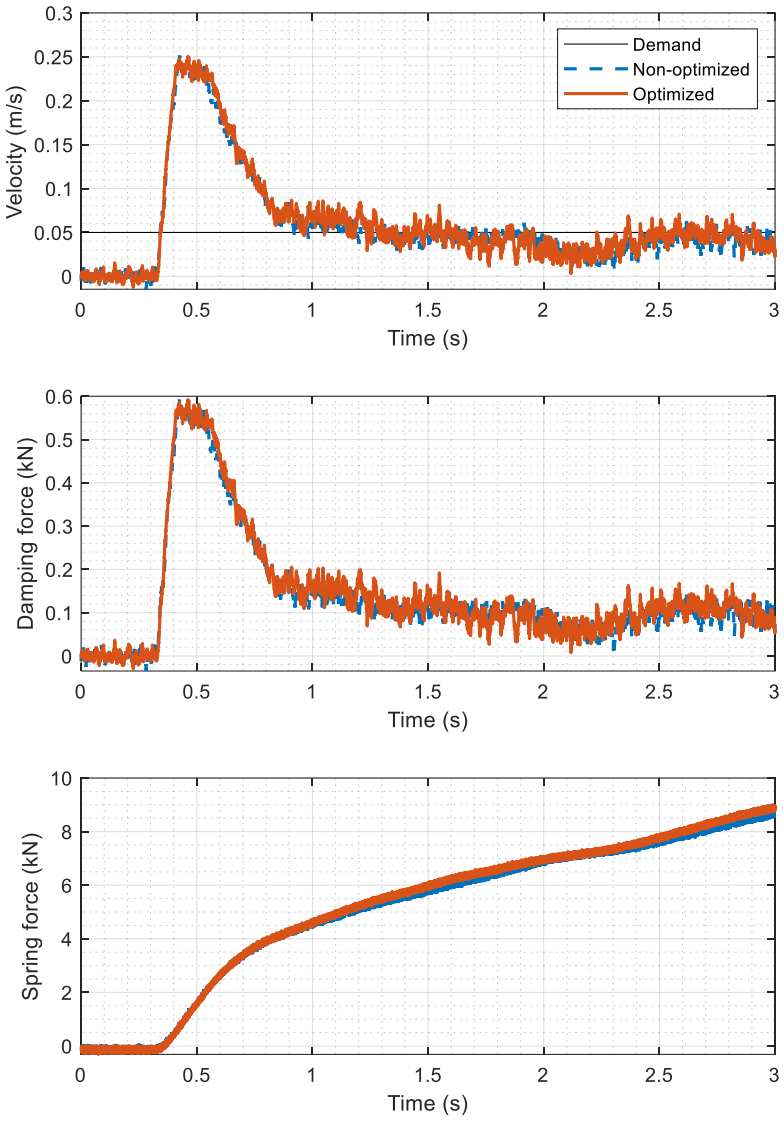

Figure 16. The velocity response, damping force, and spring force with velocity control in experiments

The switching ratio, switching frequency, and efficiency of the flow booster with velocity control are plotted in **Figure 17**. For the non-optimized result, the switching ratio saturates at 90% when the controller is turned on at 0 s because the TDCV is closed and the feedback velocity is 0 until 0.3 s. After the TDCV is open, the trolley accelerates to the maximum velocity of 0.24 m/s, which is significantly larger than the demand velocity of 0.05 m/s (see **Figure 16**). As a result, the switching ratio decreases to the low limit of 10% within 0.1 s and is constant for 0.8 s to decelerate the trolley. After that, the switching ratio gradually increases to 80% to overcome the increasing spring force. The

switching ratio of the optimized result shows a small difference due to the variation of the switching frequency. With the change of the switching ratio, the optimized switching frequency keeps constant at 30 Hz before 0.35 s, forms a peak between 0.35-0.45 s, increases to 150 Hz at 2.1 s and decreases to 75 Hz at 3 s. The optimized efficiency varies from 30% to 75%, and is improved by up to 10% compared with the non-optimized result.

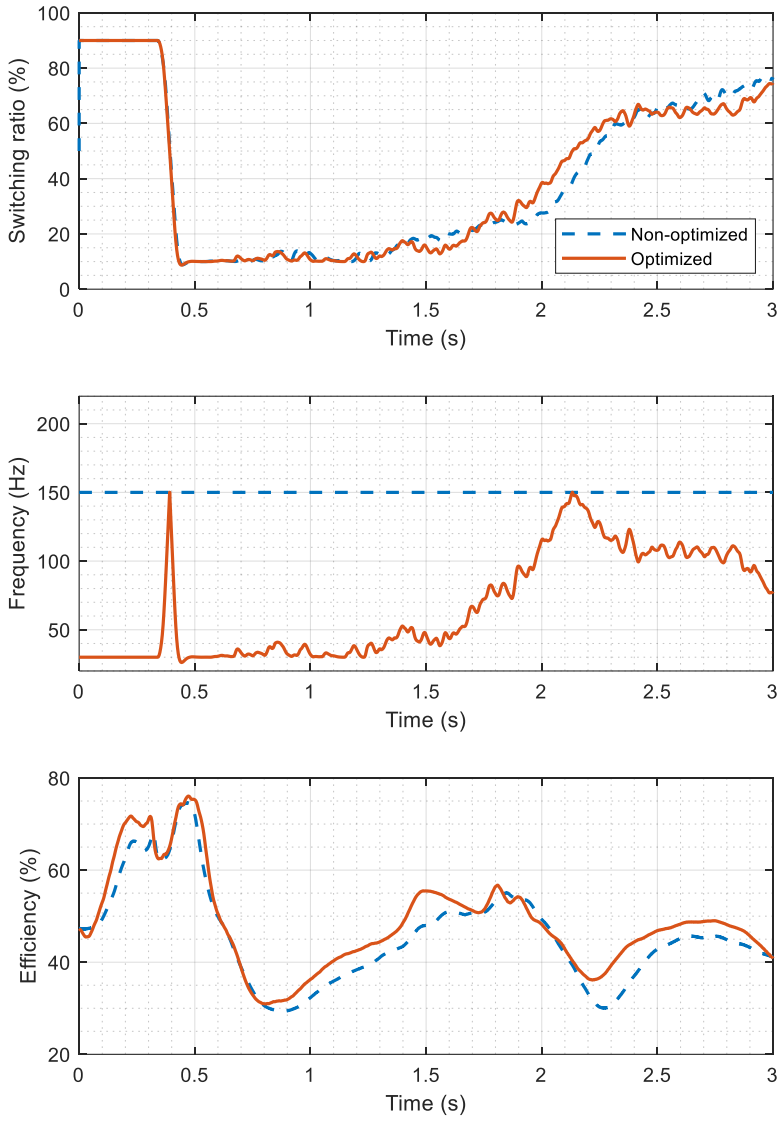

Figure 17. The switching ratio, switching frequency, and efficiency of the flow booster with velocity control in experiments

The delivery pressure and flow rate of the flow booster are shown in **Figure 18**. After the TCDV is

open, the delivery pressure of the optimized result shows a large overshoot to 36 bar at 0.4 s and increases from 20 to 46 bar to overcome the increasing spring force. Compared with the non-optimized result, up to 50% (peak-to-peak value) reduction in pressure ripple has been achieved by using the optimized controller. The delivery flow rate of the optimized result increases from 14 to 32 l/min and decreases to the steady state value of 5.5 l/min, corresponding to the demand velocity of 0.05 m/s. Due to the limited bandwidths of the flow meters, the flow ripples cannot be measured. Nonetheless, the reduction in pressure ripple validates the advantage of using the optimized controller when the load is time-varying.

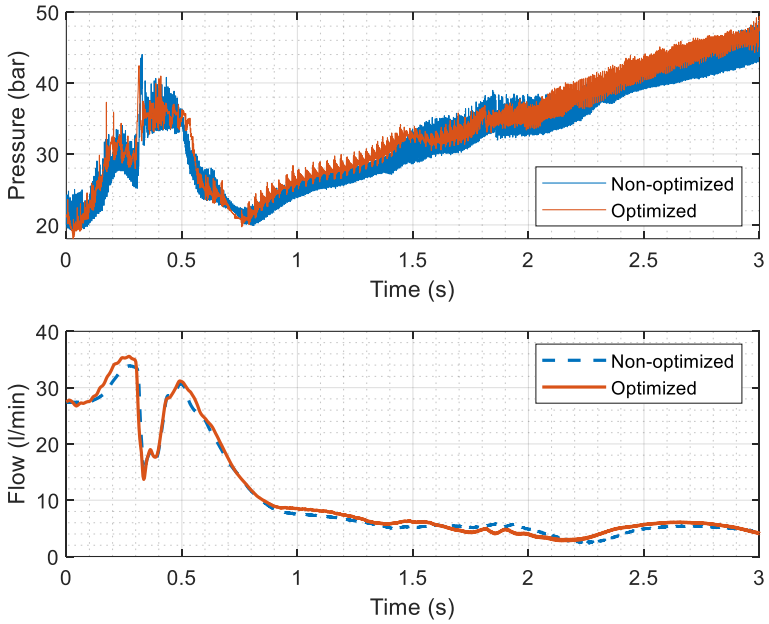

Figure 18. The delivery pressure and flow rate of the flow booster with velocity control in experiments

Figure 19 shows the piston and annulus pressures and actuator position with velocity control. When the actuator starts to move against the spring after 0.3 s, the piston pressure of the optimized result decreases to 12 bar and increases to 48 bar, while the annulus pressure increases to 20 bar before decreasing to the steady-state value of 3 bar. The actuator position achieved at 0.3 s by using the

optimized controller is 0.005 m further than that of the non-optimized result due to the improved efficiency, as explained in simulation.

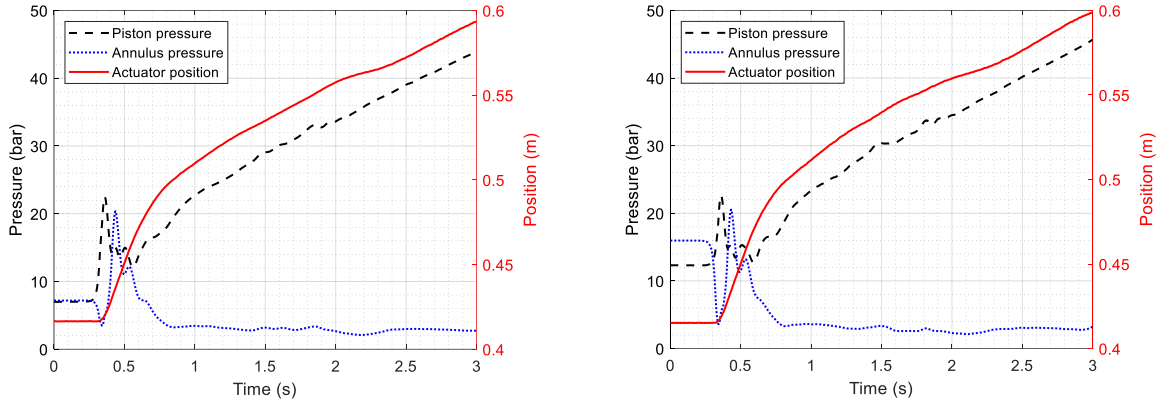

(a) Non-optimized (b) Optimized

Figure 19. The piston and annulus pressures and actuator position with velocity control in experiments

4.4.2 Force control

The actuator force feedback used for force control was calculated by:

$$F_{feedback} = P_1 A_P - P_2 A_S \tag{13}$$

Figure 20 shows the force response, damping force, and spring force with force control. The controller was turned on at 0 s, and the TDCV was opened at 0.02 s. A settling time of 1.6 s (2%) and a small overshoot of 1.4 % have been achieved by using the optimized controller, which is better compared with 1.8 s (2%) and 1.7% of using the non-optimized controller. The spring force increases from 0 kN to 8.3 kN at the steady state when the trolley stops, which is 0.7 kN less than the demand force of 9 kN. As the damping force is zero when the trolley stops at the steady state, the small difference could be the static friction force between the piston and the cylinder wall.

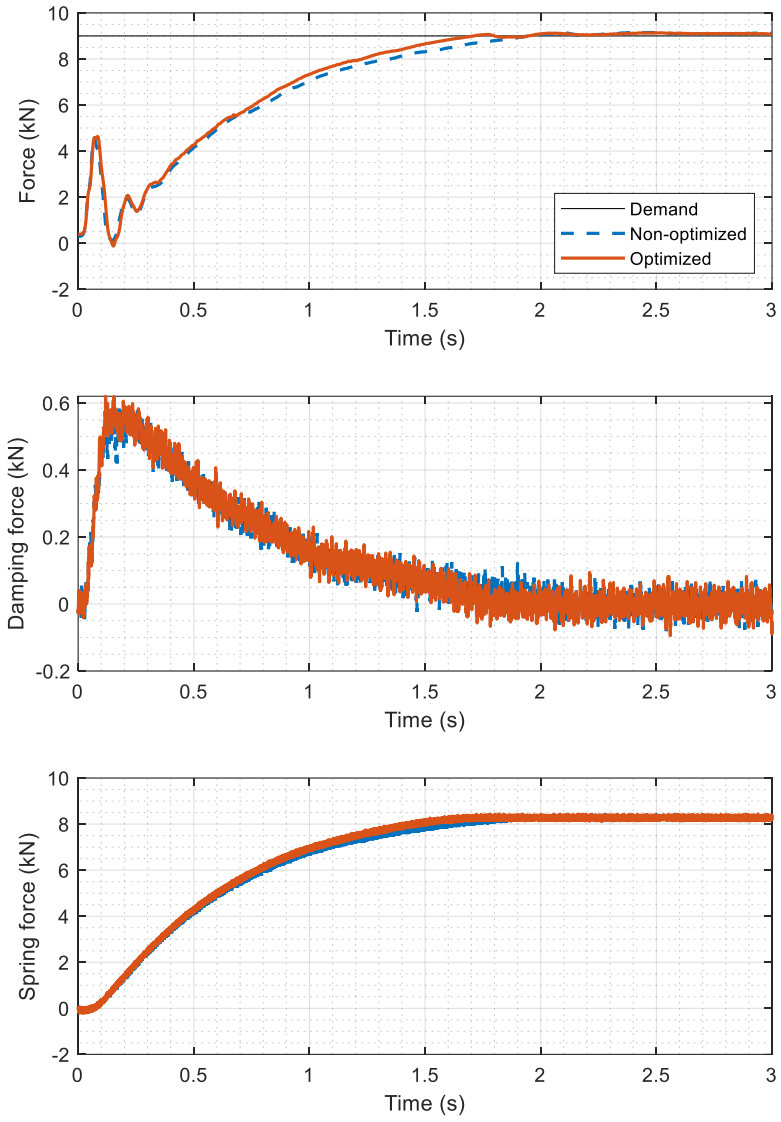

Figure 20. The force response, damping force, and spring force with force control in experiments

The switching ratio, switching frequency, and efficiency of the flow booster with force control are shown in **Figure 21**. With the optimized controller, the switching ratio maintains the maximum of 90% for 0.95 s to accelerate the trolly before decreasing to about 40% with some fluctuations. According to the variation of the switching ratio, the optimized switching frequency remains constant at 30 Hz until 1 s and increases to 150 Hz before decreasing to 110 Hz. The efficiency of the optimized result increases from 50% to 80% at 0.2 s, after which it gradually reduces to zero when the demand actuator force is balanced with the spring force and the trolley stops. The efficiency of the optimized result has been improved by up to 7%, compared with that of the non-optimized result for 0-1.5 s.

With the optimized controller, the efficiency reaches zero 0.25 s more quickly than the non-optimized result, which means that the actuator achieves the demand force, and the trolley stops more quickly. This is because it takes a shorter time to move the trolley to the balanced position due to the improved efficiency using the optimized controller.

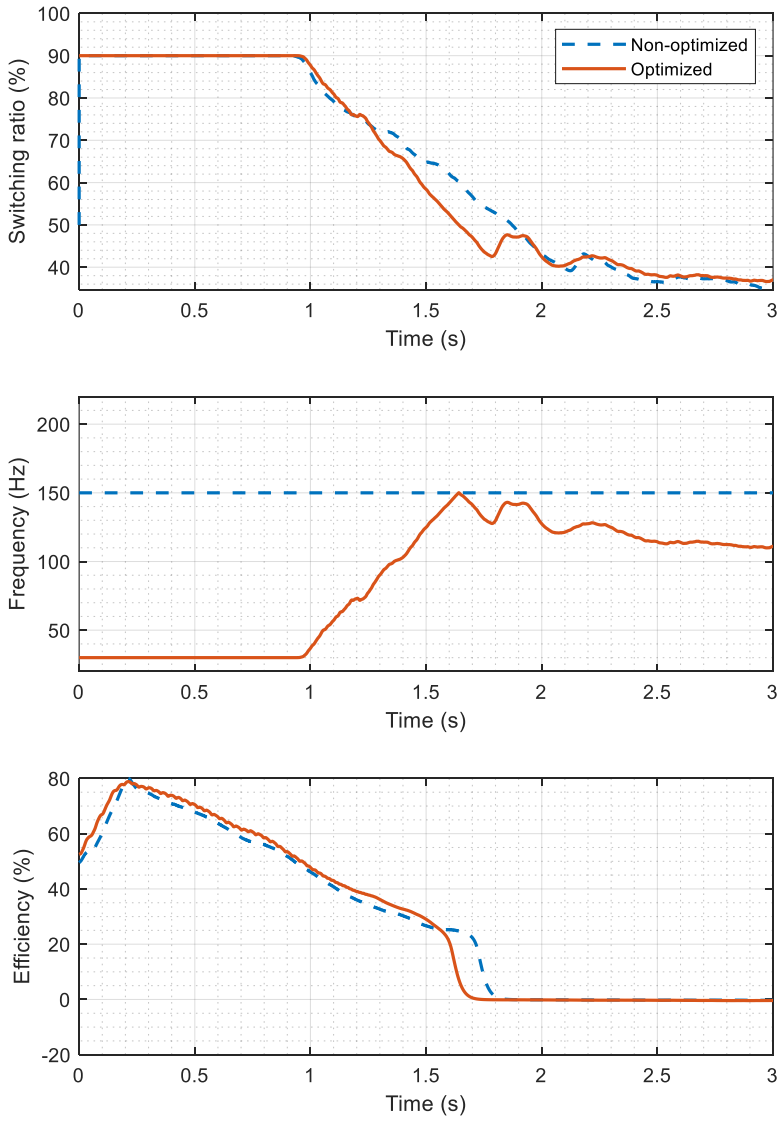

Figure 21. The switching ratio, switching frequency, and efficiency of the flow booster with force control in experiments

Figure 22 shows the delivery pressure and flow rate of the flow booster with force control. After the TDCV is open, the delivery pressure of the optimized result increases from 34 bar to about 46 bar and

maintains constant when the trolley stops moving. It is noticed that the delivery flow rate decreases quickly from 2.5 l/min to 0 l/min within 0.1 s in both results. This could be caused by the increase of the dynamic friction in the hydraulic cylinder when the velocity is lower than a threshold value (Stribeck velocity) [25-27]. The optimized controller has achieved a significant reduction (up to 65%) in the pressure ripple compared with the non-optimized result.

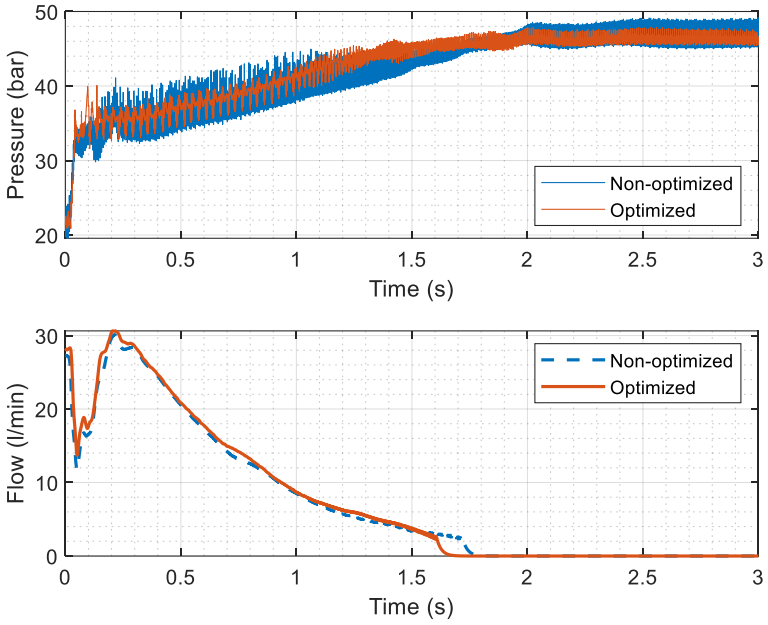

Figure 22. The delivery pressure and flow rate of the flow booster with force control in experiments

Figure 23 shows the piston and annulus pressures and actuator position of the time-varying loading system of force control. The actuator achieves the steady state at 1.75 s and 2 s for the optimized and non-optimized results, respectively, showing the quicker response of using the optimized controller due to the improved efficiency.

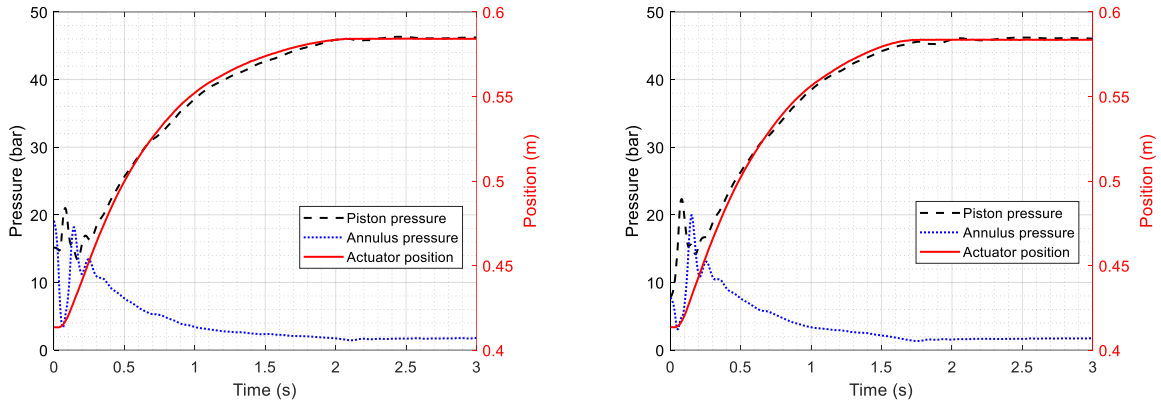

(a) Non-optimized (b) Optimized

Figure 23. The piston and annulus pressures and actuator position with force control in experiments

5. Discussion

The proposed efficient controller has shown significant improvement in pressure ripple by up to 65% and efficiency by up to 10% in experiments, compared with using the non-optimized controller. Here some concerns and possible improvements are discussed:

- Large overshoots up to 0.24 m/s were observed in velocity control at a demand of 0.05 m/s, which were caused by the initial transient due to the small spring force and damping force. The overshoots would be much smaller if a high-damping loading system was driven by the SIHC.
- The dynamic responses in velocity and force control are slow, with settling times between 1 and 2 s. This is because the high-supply pressure is relatively low (60 bar) in this study to drive a load mass of 890 kg against a spring with a stiffness of 49.14 kN/m. In addition, the system saturates at the switching ratio of 90% when accelerating and 10% when decelerating because of the saturation block in the controller. More sophisticated control could be developed to address system nonlinearities such as saturation and accumulator nonlinearity in SIHCs, for example, flatness-based control and passivity-based control developed by Kogler et al. [28-31].
- The pressure pulsation was more significant in simulation and experiments when the optimized switching frequency was 30 Hz at a 10% or 90% switching ratio. The switching frequency is too low and the pressure rises and drops more significantly with the increased time of period, which causes the large pulsation in spite of using the optimized switching frequency. A low limit of the

switching frequency, for example, 60 Hz, could be added to reduce the pulsation at switching ratios below 20% and above 80%.

- The average experimental efficiency of the optimized result at the steady state in velocity control is 46%, which is much lower than the simulated value of 76%. Due to the limit stroke (0.2 m) of the spring, a small demand velocity of 0.05 m/s was used in velocity control, corresponding to a small delivery flow rate of 5.4 l/min. The internal leakage of the rotary high-speed switching valve was found to be about 3 l/min in experiments and not included in the simulation. In this case, the internal leakage was significant relative to the small delivery flow rate and caused much lower efficiency in experiments. In comparison, the efficiencies are higher and the differences are much less significant at higher delivery flow rates (12-30 l/min, see flow rate plots at 0-0.75 s in **Figure 18** and **Figure 22**) in velocity and force control (see efficiency plots at 0-0.75 s in **Figure 17** and **Figure 21**). The efficiency could be improved by reducing the internal leakage of the switching valve and by operating the SIHC with a time-varying load requiring high delivery flow rates.
- In experiments, the length of the spring and the stroke of the actuator limits the displacement of the trolley and the spring force. Therefore, a small demand velocity and force have to be used, which corresponds to a low flow rate and pressure. The controller performance at high flow rate and pressure could be investigated in the future.
- The spring effect dominates the time-varying loading system due to the small damping in the loading system. Other loading systems could be used to study other loading effects on the controller performance, such as motors and robotic arms with effects of inertia and damping.
- In this work, the switching frequency varies with the switching ratio in real time. However, the quick change of the switching frequency is not ideal for eliminating the wave propagation effect when the load varies quickly. As in **Figure 17**, the efficiency improvement is not significant when the switching frequency significantly changes in a short time. Advanced control strategies could be proposed to control the changing rate of the switching frequency, for example, load sensing control by relating the changing rate of the switching frequency to the load change.

6. Conclusions

An efficient controller has been designed to operate the SIHC at optimized switching frequencies and switching ratios, which can reduce the pressure ripple and improve the system efficiency when the load varies. The controller integrates a PI controller and a switching frequency optimizer that calculates the optimized switching frequency when the switching ratio changes with the time-varying load to minimize the wave propagation effect. The controller performance has been numerically and experimentally validated on a flow booster with an actuator driving a mass-spring-damper system.

The proposed controller has achieved up to 10% efficiency improvement and 65% pressure ripple reduction without affecting the dynamic responses in velocity and force control, compared with using a conventional PI controller. This study proves that simultaneously controlling the switching frequencies and switching ratios of the SIHC is feasible and advantageous and enables the SIHC to adapt to the time-varying loading more efficiently and robustly. The proposed control strategy can be useful for developing high-efficiency SIHCs and their practical application in hydraulic machinery under time-varying loading conditions.

Acknowledgement

This research was funded by the RAEng/The Leverhulme Trust Senior Research Fellowship, UK, grant number LTSRF1819\15\16, the RAEng Proof-of-Concept Award PoC1920/15, the EPSRC Impact Acceleration Account institutional grant at the University of Bath, EP/X525650/1. Chenggang Yuan thanks the support from the China Scholarship Council PhD studentship (201706150102).

Declaration of Conflicting Interests

The authors declare that there is no conflict of interest.

Funding

This research was funded by the RAEng/The Leverhulme Trust Senior Research Fellowship, UK, grant number LTSRF1819\15\16, the RAEng Proof-of-Concept Award PoC1920/15, the EPSRC Impact Acceleration Account institutional grant at the University of Bath, EP/X525650/1. Chenggang Yuan thanks the support from the China Scholarship Council PhD studentship (201706150102).

References

[1] Yuan, C., Plummer, A. & Pan, M., 2021. Efficient control of a switched inertance hydraulic converter with a time-varying load. In: Proceedings of the ASME/BATH 2021 Symposium on Fluid Power and Motion Control, October 19-21 2021, Virtual, Online. p. V001T01A034.

[2] Achten, P., 2012. Discussion: Is the future of fluid power digital? *P I MECH ENG I-J SYS,* 226(I6), pp. 724-726.

[3] Yang, H.Y. & Pan, M., 2015. Engineering research in fluid power: a review. *J ZHEJIANG UNIV-SC A,* 16(6), pp. 427-442.

[4] Pan, M. & Plummer, A., 2018. Digital switched hydraulics. *Frontiers of Mechanical Engineering,* 13(2), pp. 225-231.

[5] Yuan, C., Pan, M. & Plummer, A., 2020. A review of switched inertance hydraulic converter technology. *Journal of Dynamic Systems, Measurement, and Control,* 142(5), p. 050801.

[6] Brandstetter, R., Deubel, T., Scheidl, R., Winkler, B. & Zeman, K., 2017. Digital hydraulics and "Industrie 4.0". *P I MECH ENG I-J SYS,* 231(2), pp. 82-93.

[7] Yuan, C., Mao Lung, V.L., Plummer, A. & Pan, M., 2020. Theoretical and experimental studies of a digital flow booster operating at high pressures and flow rates. *Processes,* 8(2), p. 211.

[8] Pan, M., Johnston, D.N., Plummer, A., Kudzma, S. & Hillis, A., 2014. Theoretical and experimental studies of a switched inertance hydraulic system. *Proceedings of the Institution of Mechanical Engineers, Part I: Journal of Systems and Control Engineering,* 228(1), pp. 12-25.

[9] Brown, F.T., 1987. Switched reactance hydraulics: a new way to control fluid power. In: National Conference on Fluid Power, 1987. pp. 25-33.

[10] Brown, F., Tentarelli, S. & Ramachandran, S., 1988. A hydraulic rotary switched-inertance servo-transformer. *Journal of Dynamic Systems, Measurement, and Control,* 110(2), pp. 144-150.

[11] Liaw, C.-J. & Brown, F., 1990. Nonlinear dynamics of an electrohydraulic flapper nozzle valve. *Journal of Dynamic Systems, Measurement, and Control,* 112(2), pp. 298-304.

[12] Kogler, H. & Scheidl, R., 2008. Two basic concepts of hydraulic switching converters. In: The First Workshop on Digital Fluid Power, October 3rd 2008, Tampere, Finland. pp. 7-30.

[13] Kogler, H., Scheidl, R., Ehrentraut, M., Guglielmino, E., Semini, C. & Caldwell, D.G., 2010. A compact hydraulic switching converter for robotic applications. In: Proceedings of the ASME/BATH 2010 Symposium on Fluid Power and Motion Control, September 15-17 2010, Bath, UK. pp. 55-66.

[14] Guglielmino, E., Semini, C., Yang, Y.S., Caldwell, D., Kogler, H. & Scheidl, R., 2009. Energy efficient fluid power in autonomous legged robotics. In: Proceedings of the ASME 2009 Dynamic Systems and Control Conference, October 12-14 2009, Hollywood, California, USA. pp. 1759-1766.

[15] Guglielmino, E., Semini, C., Kogler, H., Scheidl, R. & Caldwell, D.G., 2010. Power hydraulics-switched mode control of hydraulic actuation. In: Intelligent Robots and Systems (IROS), 2010 IEEE/RSJ International Conference on, 2010. IEEE, pp. 3031-3036.

[16] Peng, S., Kogler, H., Guglielmino, E., Scheidl, R., Branson, D.T. & Caldwell, D.G., 2013. The use of a hydraulic DC-DC converter in the actuation of a robotic leg. In: 2013 IEEE/RSJ International Conference on Intelligent Robots and Systems (IROS), November 3-7 2013, Tokyo, Japan. pp. 5859-5864.

[17] Wang, P., Kudzma, S., Johnston, N., Plummer, A. & Hillis, A., 2011. The influence of wave effects on digital switching valve performance. In: The Fourth Workshop on Digital Fluid Power, September 21-22 2011, Linz, Austria. pp. 10-25.

[18] Pan, M., Johnston, N., Plummer, A., Kudzma, S. & Hillis, A., 2014. Theoretical and experimental studies of a switched inertance hydraulic system including switching transition dynamics, non-linearity and leakage. *Proceedings of the Institution of Mechanical Engineers, Part I: Journal of Systems and Control Engineering,* 228(10), pp. 802-815.

[19] Pan, M., Johnston, N., Robertson, J., Plummer, A., Hillis, A. & Yang, H.Y., 2015. Experimental investigation of a switched inertance hydraulic system with a high-speed rotary valve. *Journal of Dynamic Systems, Measurement, and Control,* 137(12), p. 121003.

[20] Åström, K.J., Hägglund, T. & Astrom, K.J., 2006. *Advanced PID control*. Research Triangle Park, NC 27709: International Society of Automation.

[21] Krus, P., Weddfelt, K. & Palmberg, J.-O., 1994. Fast pipeline models for simulation of hydraulic systems. *Journal of Dynamic Systems, Measurement, and Control,* 116(1), pp. 132-136.

[22] Johnston, N., 2012. The transmission line method for modelling laminar flow of liquid in pipelines. *P I MECH ENG I-J SYS,* 226(5), pp. 586-597.

[23] Johnston, D.N. & Edge, K.A., 1991. In-Situ Measurement of the Wavespeed and Bulk Modulus in Hydraulic Lines. *Proceedings of the Institution of Mechanical Engineers, Part I: Journal of Systems and Control Engineering,* 205(3), pp. 191-197.

[24] Yuan, C., Plummer, A. & Pan, M., 2022. Switching characteristics of a high-speed rotary valve for switched inertance hydraulic converters. *Proceedings of the Institution of Mechanical Engineers, Part I: Journal of Systems and Control Engineering*.

[25] Armstrong-Hélouvry, B., Dupont, P. & De Wit, C.C., 1994. A survey of models, analysis tools and compensation methods for the control of machines with friction. *AUTOMATICA,* 30(7), pp. 1083-1138.

[26] Haessig, D.A., Jr. & Friedland, B., 1991. On the modeling and simulation of friction. *Journal of Dynamic Systems, Measurement, and Control,* 113(3), pp. 354-362.

[27] Tran, X., Khaing, W., Endo, H. & Yanada, H., 2014. Effect of friction model on simulation of hydraulic actuator. *Proceedings of the Institution of Mechanical Engineers, Part I: Journal of Systems and Control Engineering,* 228(9), pp. 690-698.

[28] Kogler, H. & Scheidl, R., 2015. Linear motion control with a low-power hydraulic switching converter-Part I: Concept, test rig, simulations. *Proceedings of the Institution of Mechanical Engineers, Part I: Journal of Systems and Control Engineering,* 229(8), pp. 677-684.

[29] Kogler, H. & Scheidl, R., 2015. Linear motion control with a low-power hydraulic switching converter-Part II: Flatness-based control. *Proceedings of the Institution of Mechanical Engineers, Part I: Journal of Systems and Control Engineering,* 229(9), pp. 818-828.

[30] Kogler, H. & Scheidl, R., 2016. Energy efficient linear drive axis using a hydraulic switching converter. *Journal of Dynamic Systems, Measurement, and Control,* 138(9), p. 091010.

[31] Kogler, H., Schöberl, M. & Scheidl, R., 2019. Passivity-based control of a pulse-width mode operated digital hydraulic drive. *Proceedings of the Institution of Mechanical Engineers, Part I: Journal of Systems and Control Engineering,* 233(6), pp. 656-665.